Balancing fracture toughness and transparency in barium titanosilicate glass-ceramics

Sun, Daming; Zhang, Qi; Liu, Pengfei; Jensen, Lars R.; Wang, Deyong; Smedskjær, Morten Mattrup

Published in:
Ceramics International

DOI (link to publication from Publisher):
10.1016/j.ceramint.2023.02.115

Publication date:
2023

Document Version
Publisher's PDF, also known as Version of record

Ceramics International 49 (2023) 17479–17487

Contents lists available at ScienceDirect

Ceramics International

journal homepage: www.elsevier.com/locate/ceramint

Balancing fracture toughness and transparency in barium titanosilicate glass-ceramics

Daming Sun [a], Qi Zhang [a], Pengfei Liu [a], Lars R. Jensen [b], Deyong Wang [b], Morten M. Smedskjaer [a,*]

[a] Department of Chemistry and Bioscience, Aalborg University, Aalborg, Denmark
[b] Department of Materials and Production, Aalborg University, Aalborg, Denmark

ARTICLE INFO

Handling Editor: Dr P. Vincenzini

Keywords:
Oxide glass-ceramics
Microstructure
Transparency
Fracture toughness
Toughening mechanism

ABSTRACT

Tough and hard, yet transparent materials are needed for a range of applications. Here, we study the effect of crystallization on the mechanical and optical properties of barium titanosilicate glass-ceramics. We characterize the morphology and size of crystals to reveal the relationship between crystallinity, transparency, and mechanical properties. We find that the size and content of crystals increase upon heat-treatment of the precursor glass, which leads to an increase in fracture toughness (from 0.7 to 0.9 MPa $m^{1/2}$) and hardness (from 5.8 to 6.6 GPa), reflecting that crystals hinder the propagation of cracks and that the glass-ceramics feature more bond constraints per unit volume, thereby improving the fracture toughness and hardness. There is a decrease in the crack initiation resistance. The transmittance decreases significantly upon crystallization due to light scattering. In conclusion, our study reveals a trade-off between fracture toughness and transparency in this series of glass-ceramics.

1. Introduction

Nanostructured materials have been widely studied due to their size, surface (interface), and macroscopic quantum tunneling effects [1–3]. This also includes glass materials with nanostructures as these can exhibit improved dielectric properties, thermal shock resistance, ferroelectricity, fluorescence, nonlinear optical properties and importantly, mechanical properties compared to the standard homogeneous glasses [4–8]. To this end, controlled crystallization of a precursor glass to form a glass-ceramic is one of the widely used methods for preparing glasses with nanostructures. Glass-ceramics have found use in several applications, including microelectronic packing and optical devices [9–11]. An important challenge for many applications is the need to prepare optically transparent glass-ceramics [12–14]. Glass-ceramics are usually opaque owing to the refraction of light by the crystal boundaries, but if the crystal size is sufficiently small or the refractive index of the glass and crystal phases match, it is possible to prepare transparent glass-ceramics (TGCs) [15–18]. The preparation of transparent glass-ceramics thus requires careful control of the heat-treatment conditions [19] or the use of other methods to control crystal formation (e.g., laser irradiation) [20].

The mechanical and light transmission properties can be changed by controlling the content, size, and orientation of the crystals in the glass-ceramics. For example, Luo et al. [21] have shown that increasing the content of SiO_2 in LiO_2–Al_2O_3–SiO_2 glass-ceramics increases the hardness and crack resistance due to the formation of interlocking microstructures. However, increasing the content of SiO_2 changes the crystal type from β-spodumene to diopside, resulting in further devitrification of the glass-ceramic. The metasilicate phase produced in glass-ceramics with high LiO_2 content also leads to translucent or opaque samples. Controlling the composition is thus a key to the preparation of transparent glass-ceramics. Gallo et al. [22] have investigated the mechanical properties of MgO–Al_2O_3–SiO_2 glass-ceramics, finding an increase in hardness and fracture toughness upon crystallization. The higher fracture toughness was ascribed to the compositional change of the residual glass phase as well as the more tortuous crack paths among small crystals. Fu et al. [23] have prepared glass-ceramics with high transparency and high toughness by forming highly anisotropic crystals and matching the refractive index of the lithium disilicate glass crystal with that of the glass phase. Overall, these previous studies suggest that larger crystal size and crystals with higher aspect ratio can increase fracture toughness, but typically at the expense of reduced transparency.

* Corresponding author.
E-mail address: mos@bio.aau.dk (M.M. Smedskjaer).

https://doi.org/10.1016/j.ceramint.2023.02.115
Received 18 December 2022; Received in revised form 10 February 2023; Accepted 14 February 2023
Available online 16 February 2023

Glass-ceramics based on the $BaO–TiO_2–SiO_2$ (BTS) system have been extensively studied due to the excellent dielectric and nonlinear optical properties of fresnoite $Ba_2TiSi_2O_8$ crystals [24,25]. Numerous studies have shown that BTS glass-ceramics can produce *c*-axis oriented crystals on the glass surface after heat treatment [26,27]. Based on the perovskite phase of $Ba_2TiSi_2O_8$ crystals, BTS glass-ceramics are often fabricated for use as nonlinear optical materials and electronic ceramic materials [28]. Fresnoite $Ba_2TiSi_2O_8$ belongs to the P4bm group and has a TiO_5 square cone structure, which causes the polarizability of the crystal [29,30]. Therefore, BTS crystals produced by heat treatment are anisotropic and tend to grow along the c-axis. However, the mechanical properties of BTS glass-ceramics have not yet been fully understood, although a few studies have been reported. Shinozaki et al. [31] have shown that increasing the crystal content in BTS glass-ceramics can increase the elastic modulus and hardness. The indentation fracture toughness also increases with increasing crystallite content, from 0.48 to 1.04 MPa $m^{1/2}$. Ghardi et al. [32] reported that increasing the TiO_2 content can increase the modulus of BTS glasses. The fact that only few studies on the mechanical properties of BTS glass-ceramics exist may be because the current applications focus on their luminescent and dielectric properties, while mostly ignoring the possible applications within, e.g., packaging. Masai et al. [49] studied the transparency of BTS glass-ceramics with different compositions, showing that the chemical composition has a great influence on the transmission properties after heat treatment.

Here, we focus on synthesizing transparent BTS glass-ceramics containing nanocrystals to further clarify the crack initiation and propagation behaviors of BTS glass-ceramics. In previous work, Yoorim et al. [33] investigated the impact of heat-treatment temperature (between T_g and T_p, where T_g is the glass transition temperature and T_p is the peak crystallization temperature) on the crystallization of a $30.77BaO\text{-}15.38TiO_2\text{-}53.85SiO_2$ glass. By fitting a Gaussian equation to the T_p data of glass-ceramics treated at different temperatures, an optimum nucleation temperature was found to be 829 °C. In this work, we slightly increased the SiO_2 content compared to this previous investigation to better balance the mechanical properties and light transmittance, as higher transparency in BTS glass-ceramics has been found upon increasing the content of SiO_2 [27,49,54]. Specifically, we have prepared a precursor $30BaO–15TiO_2–55SiO_2$ glass that is heat treated at 860 °C for 2 h, 4 h and 8 h to prepare glass-ceramics with different crystal fractions and sizes. The morphology, size, and content of crystals in glass-ceramics are characterized by scanning electron microscopy and x-ray diffraction, and the glass matrix structure is examined using Raman spectroscopy. The mechanical properties are tested by ultrasonic echography to measure elastic moduli and micro-indentation to measure hardness, crack initiation resistance, and indentation fracture toughness. We also determine fracture toughness using the single edge pre-crack beam method.

2. Experimental

2.1. Sample preparation

A transparent glass with composition $30BaO–15TiO_2–55SiO_2$ was prepared by the traditional melt-quenching method. The raw materials were $BaCO_3$ (≥99%, Sigma-Aldrich), TiO_2 (≥99%, Honeywell International) and quartz (fine granular, 99.95%, Sigma-Aldrich). The mixed powders were added to PtRh crucibles, melted, and homogenized in an electric furnace at 1550 °C for 2 h. Then, the molten mixture was poured onto a brass plate and quenched with a steel plate. To improve homogeneity, the quenched glass was crushed and remelted for another 1 h. Finally, this melt was quenched, and the obtained glass was transferred to an annealing furnace at an estimated glass transition temperature (T_g) for 30 min. After annealing, the sample was cooled down to room temperature in the furnace at a rate of about 2 K/min. The actual T_g of the BTS glass was subsequently determined by differential scanning calorimetry (DSC, STA 449 F3 Jupiter, Netzsch). To this end, the annealed glass was polished to a thickness of 1 mm, put into a Pt crucible, and heated to 950 °C at a rate of 10 K/min under an Ar flow (flow rate of 40 mL/min). The DSC curve is shown in Supporting Fig. S1, where we defined the T_g as the temperature corresponding to the crossing point between the tangent of the inflection point of the internal heat peak and the extrapolated heat flow of the glass. The measured T_g value was 743 °C, while T_p (crystal growth maximum rate temperature) was found to be 1024 °C. After the DSC measurement, the glass was annealed for 30 min at this temperature and then cooled down in the furnace.

Based on Yoorim's work [33], we here used the same method and tested the T_p of BTS glass-ceramics heat-treated at different temperatures of (800 °C, 850 °C, 900 °C, and 950 °C, respectively (results not shown), and finally set the heat treatment temperature to 860 °C. The heat-treatment experiments were done on samples cut to dimensions of $1 \times 1.5 \times 0.3$ cm^3. Specifically, the furnace was preheated to 860 °C at a rate of 10 K/min, and then the sample was inserted in the furnace and heat-treated for 2, 4, or 8 h. After annealing, the sample was cooled down to room temperature in the furnace at a rate of about 2 K/min. We note that for BTS glass-ceramics, faster cooling rates lead to tensile stresses in the glass-ceramics due to thermal expansion mismatch [34,35]. To avoid this effect, a lower rate was used for cooling after heat treatment in this work. Then, we ground the surface to remove the top ~0.1 mm layer to remove the impact of surface crystallization. These samples were then polished using SiC sandpaper (from 200 to 4000 grit).

2.2. Glass and crystal structures

The surface morphologies of both the glass and glass-ceramic samples were characterized using field emission scanning electron microscopy (SEM, Zeiss 1540XB). Before the analyses, the sample surfaces were etched with 1 wt% hydrofluoric acid for 10 s and then coated with gold. To observe differences in the crack propagation paths in the precursor glass and glass-ceramics samples, we also used SEM to observe the propagation paths of cracks induced by indentation (see details on indentation experiments in Section 2.5). The operating voltage of the SEM was 10 kV. In this case, the surface of the samples were not etched to observe the crack propagation path.

Phase detection in the glass-ceramic samples was carried out using x-ray diffraction (Empyrean XRD, PANalytical) with monochromatic Cu Kα radiation. The scanning angle of XRD was set from 5° to 75°, the scanning current was 40 mA, the voltage was 40 kV, and the scanning speed was 1.75°/min. The short-range and medium-range structures of the glasses were characterized by Raman spectroscopy. The Raman spectra were acquired on a micro-Raman spectrometer (inVia Renishaw) with an objective aperture of 0.75, a laser of 532 nm and an acquisition time of 10 s [36]. The spectral range was from 200 to 1400 cm^{-1}. Each sample was tested on three different locations to verify their homogeneity. All spectra were finally subjected to background correction and area normalization.

2.3. Transmission properties

To study the effect of crystal content and size on the transparency of the glass-ceramic samples, we performed ultraviolet–visible (UV–vis) spectrometer measurements (Cary 50 Bio, Varian) in transmission mode on double-side polished samples. We measured the baseline-corrected transmittance of the samples from 255 to 800 nm wavelength with the scanning speed of 60 nm/min. The transmittance was calculated from the absorption data, and the spectral data were all normalized to 1 mm thickness. Three different areas were tested to ensure the reliability of the obtained results.

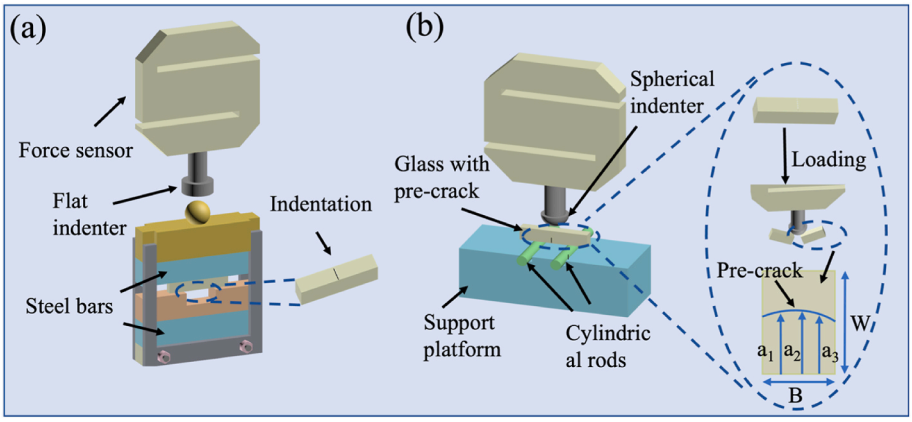

Fig. 1. Schematic diagram of the SEPB method for fracture toughness determination. (a) Pre-cracking process of the glass sample using the bridge compression fixture, where the loading rate of the flat indenter is 0.05 mm/min. (b) Three-point bending test, where the loading rate of the indenter is 0.9 mm/min. After fracture, the pre-crack length was measured as $a = (a_1+a_2+a_3)/3$.

2.4. Ultrasonic echography

The density (ρ) was determined using Archimedes method. The sample was first weighed on the balance in air (m_1) and then weighted again while immersed in absolute ethanol ($\rho = 0.791$ g/cm^3) to obtain the mass as m_2. Each sample was repeatedly measured ten times, and finally the density was calculated as,

$$\rho_{Glass} = \frac{m_1 * \rho_{Ethanol}}{m_1 - m_2} \tag{1}$$

Young's modulus of the precursor glass was then measured using an ultrasonic thickness gauge (38 DL Plus, Olympus) equipped with a 20 MHz piezoelectric transducer to generate sound waves. The velocity of the transverse acoustic wave (V_T) and the longitudinal acoustic wave (V_L) were measured by the pulse-back method. In combination with the density (ρ), the longitudinal modulus C_{11}, Young's modulus (E), shear modulus (G), bulk modulus (K) and Poisson's ratio (υ) can be calculated as follows:

$$C_{11} = \rho V_L^2 \tag{2}$$

$$G = \rho V_T^2 \tag{3}$$

$$K = C_{11} - \frac{4}{3}G \tag{4}$$

$$\upsilon = \frac{3K - 2G}{6K + 2G} \tag{5}$$

$$\mathrm{E} = 2\mathrm{G} + 2\mathrm{G}\upsilon \tag{6}$$

2.5. Indentation

Vickers hardness (H_V), crack initiation resistance (CR) and indentation fracture toughness (K_{IFT}) of the samples were measured by micro-indentation (CB500, Nanovea). For hardness tests, we used a Vickers diamond tip (four-sided pyramid-shaped diamond with an angle of 136°) to produce indents at a load of 0.98 N on each sample, with a loading speed of 9.8 N/min, and a holding time of 6 s 15 indents were analyzed for each sample. The lengths d_1 and d_2 of the two indent diagonals were measured using an optical microscope (Olympus) and then H_V was calculated.

The CR value corresponds to the load value with a probability of cracking of 50% [37,38]. Specifically, the initiation probability of crack initiation is defined as the ratio between the number of cracked corners and the total number of corners during the test. The measurement of CR was also done using the Vickers tip, but here we used varying peak loads. The number of corners with cracks after unloading at different load and different loading rate (loading rate (in N/min) was equal to ten times the numerical value of the load (in N), while holding time was 6 s) were observed using a microscope. The indentations were performed under laboratory conditions (23 °C, ~40% relative humidity). The ratio between the number of cracked corners and the total number of corners was recorded for each load 1 h after unloading. For each sample and load, 15 indents were analyzed.

The indentation fracture toughness (K_{IFT}) was also determined. However, the determination of K_{IFT} from Vickers indentation is problematic, e.g., due to densification that is not accounted for in the calculation [40]. Following Ref. [39], to obtain a more reliable estimation of the indentation fracture toughness, we here used a sharper 100° four-sided pyramidal tip (instead of the 136° Vickers tip) to reduce the densification component of the deformation. The applied load was 0.98 N, and the holding time was 6 s. After unloading, we observed the indentation morphology under a microscope, recorded the diagonal length of the indent and the length of the crack at each indentation corner. We measured 30 indents for each sample and then calculated indentation fracture toughness as,

$$K_{\mathrm{IFT}} = 0.035\left(\frac{E}{H_V}\right)^{\frac{1}{2}}\left(\frac{P}{{c_0}^{3/2}}\right) \tag{7}$$

where E is the Young's modulus, Hv is the Vickers hardness calculated under the 100-degree indenter, P is the load, and c_0 is half of the average crack length. The coefficient depends on the tip geometry and was here set to 0.035 for the 100° four-sided pyramidal tip [41].

2.6. Single-edge precracked beam

The fracture toughness (K_{Ic}) was measured based on the single-edge precracked beam (SEPB) method, which included two steps, namely the generation of pre-crack (Fig. 1a) and three-point bending test (Fig. 1b). The measurements were performed on samples with dimensions of 1 mm $\leq B \leq$ 2 mm, 2 mm $\leq W \leq$ 3 mm, $L \geq$ 10 mm, where B is the broadness, W is the width, and L is the length. The results measured on such relatively small samples have been shown to provide consistent results [42,43]. First, we cut the samples with a diamond cutting machine (Secotom-60, Struers). The cutting speed and feed speed were 100 rpm and 0.05 mm s^{-1}, respectively, to obtain samples with dimensions of 1.5 × 2 × 10 mm^3 after polishing all sides of the samples with SiC paper of different abrasive particle size (from 320 to 4000 grit). After polishing, the B sides of the samples were subjected to indentation to form five to ten Vickers indents at a load of 9.8 N, which was sufficient to generate corner cracks. To form the precrack through the growth of

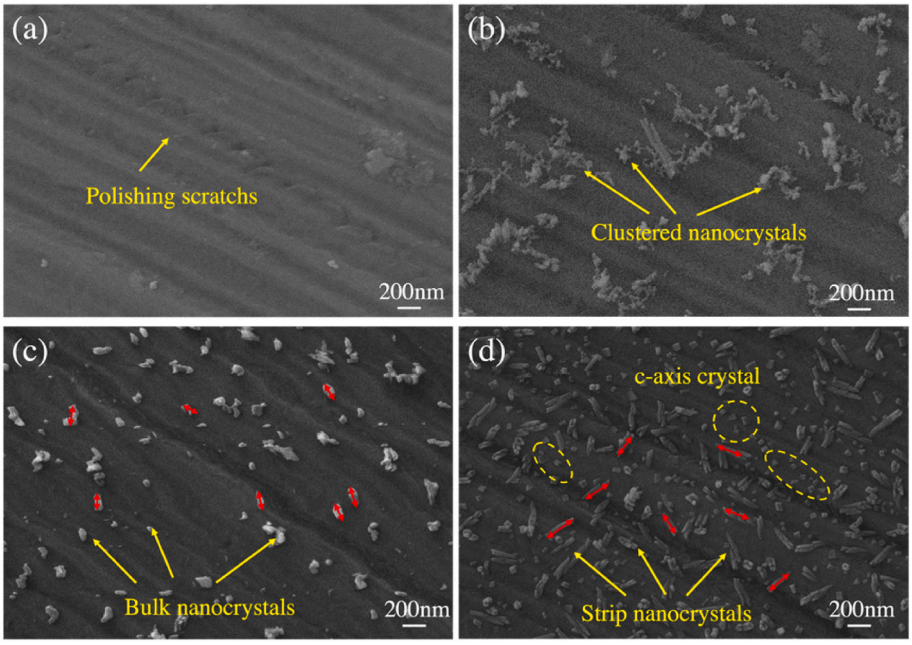

Fig. 2. SEM images of (a) precursor glass and (b–d) glass-ceramics heat-treated at (b) 860°C-2h, (c) 860°C-4h, and (d) 860°C-8h. The magnification is 30,000 times.

corner-crack of these indentations, we placed the samples in a bridge compression fixture as shown in Fig. 1a. Firstly, the indented side of the sample was faced down in the center of the groove (length of groove was 4 mm). Then, a compressive load was applied to the fixture with a universal testing machine (Z100, Zwick, with 100 kN load cell) and a loading rate of 0.05 mm/min. The cracks on the surface with indentation began to grow and became connected and then propagated until it reached the middle of the specimen width. Finally, we obtained a pre-crack with the size of ~0.5W.

Fig. 1b shows a schematic diagram of a three-point bending test. The precracked samples were subjected to three-point bending and fractured by using a cross-head speed of 0.9 mm/min. All fracture samples were collected after testing in order to measure the pre-crack length (a). The pre-crack length of the sample was determined through light optical microscopy, where three points were measured in the middle of the crack (see details in the bottom of the dotted circle in Fig. 1b), and the average value was taken as the pre-crack length. The maximum load P_{max} during the loading process was determined by the load cell, which was used to calculate K_{Ic} [44],

$$K_{Ic} = \frac{P_{max}}{B\sqrt{W}} Y^* \tag{8}$$

$$Y^* = \frac{3S}{2W} \frac{\sqrt{\alpha}}{\sqrt[2]{(1-\alpha)^3}} f(\alpha) \tag{9}$$

where P_{max} is the peak load during the loading process, B and W are the breadth and width of the sample, respectively, α is the ratio of pre-crack to width (a/W, $a=(a_1+a_2+a_3)/3$), $f(\alpha) = [1.99-(\alpha-\alpha^2)*(2.15–3.93\alpha+2.7\alpha^2)]/(1+2\alpha)$ for $S/W = 4$, $f(\alpha) = 1.9109 - 5.1552\alpha + 12.6880\alpha^2 - 19.5736\alpha^3 + 15.9377\alpha^4 - 5.1454\alpha^5$ for $S/W = 5$. S is the distance of adapted three-point bending span (here 8 mm). The fracture toughness was measured five times for each sample.

3. Results and discussion

3.1. Phase identification

The crystal size, content, and distribution uniformity can influence the properties of the glass-ceramics, for example rapid grain growth during crystal growth can result in reduced transparency [46]. The crystal morphology as determined by SEM is shown in Fig. 2. As shown in Fig. 2a, there are no crystals in the precursor glass. With the increase of heat-treatment time, crystals appear in the BTS glass matrix, and the crystal size and content increase. In addition, with the extension of the heat-treatment time, the crystal morphology changes. Upon 2 h heat-treatment, the crystals are small and tend to form clusters randomly distributed in the matrix. Although the clustered nanocrystals in Fig. 2b appear to be larger than the bulk nanocrystals, they are less widely distributed in the glass-ceramics. The heat treatment time of 2 h is insufficient to make them fully agglomerate and grow extensively, and their content is thus below the detection threshold of XRD. This phenomenon has previously been reported in other glass-ceramics systems [47]. When the heat-treatment time increases to 4 h, the crystal size increases (average 131 nm, Fig. 2c, red arrow), the crystal morphology becomes more irregular, and the crystal density increases. When the

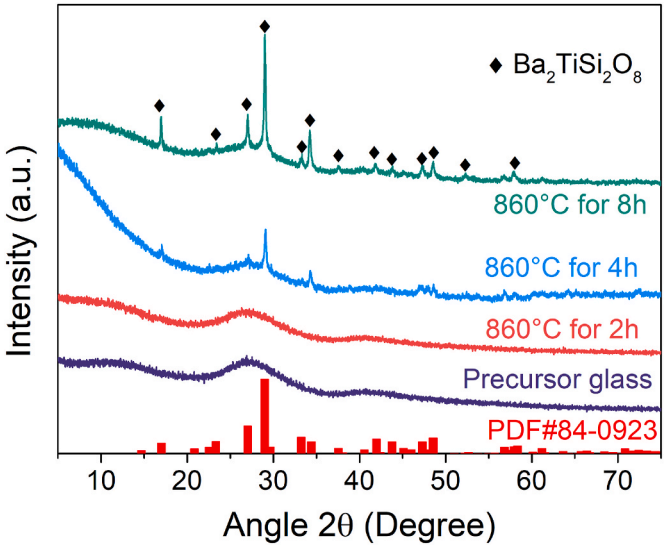

Fig. 3. XRD patterns of precursor glass and glass-ceramic samples. PDF card #84–0923 corresponds to the fresnoite $Ba_2TiSi_2O_8$ crystal.

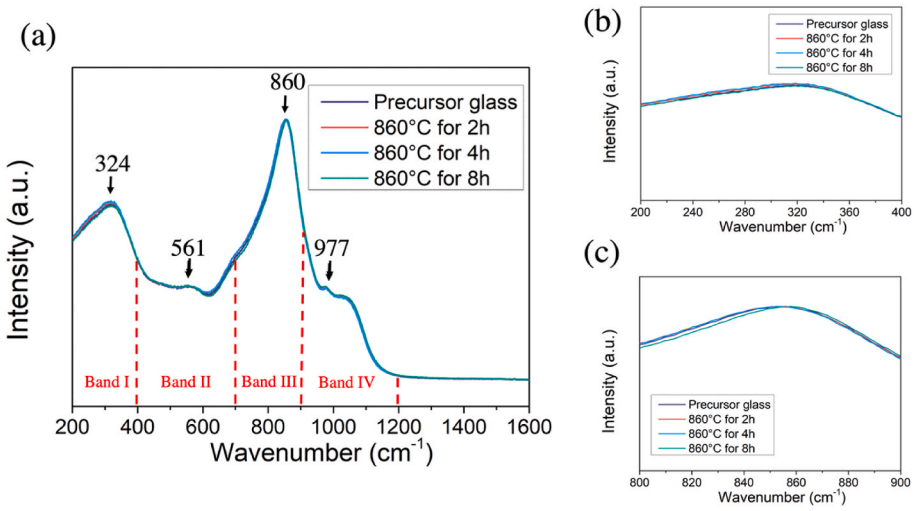

Fig. 4. (a) Raman spectra of the precursor glass and the glass-ceramics. (b) and (c) shown the Raman spectra in the 200-400 cm^{-1} and 800-900 cm^{-1} band regions, respectively.

heat-treatment time is further extended to 8 h, the crystals shape changes from irregular lumps to longer strips, the average size increases to 274 nm, and the crystal density further increases (Fig. 2d). It can be clearly seen in the 8 h heat-treated sample that the BTS glass-ceramics with non-stoichiometric ratios (i.e., glass and crystal have different compositions) have c-axis oriented $Ba_2TiSi_2O_8$ crystals (yellow dashed circle) [48].

Fig. 3 shows the XRD patterns of the present samples, as well as the fresnoite $Ba_2TiSi_2O_8$ standard PDF card. The precursor glass and the sample heat-treated for 2 h have no sharp diffraction peaks. Note that we removed a thickness of about 0.1 mm from the surface of the sample before characterization, but there was also no excessive crystal growth on the surface of the sample heat-treated for 2 h prior to polishing (Supporting Fig. S2). This may be due to (1) the small size of the crystal below the detection threshold, or (2) insufficient heat treatment time leads to thinner crystal layers [49]. After prolonging the heat-treatment time to 4 and 8 h, crystalline diffraction peaks appear. The diffraction intensity of the main peak at 29° is highest after 8 h treatment and the intensity of the broad amorphous peak decreases. All the diffraction peaks can be assigned to the fresnoite single crystal diffraction pattern, which shows that extending the heat treatment time can form crystals inside the glass, and *c*-axis oriented crystals tend to form in non-stoichiometric BTS glasses [50].

Fig. 4 shows Raman spectra of the samples, revealing only minor changes upon heat-treatment. Based on the previous studies, we divided the spectrum into four main band regions. The bands below 400 cm^{-1} (Fig. 4b) are difficult to clearly assign because of the presence of external modes as well as bending modes of Si_2O_7 and TiO_5 groups [50], and we therefore do not consider them further herein. The Raman peaks in the 400-700 cm^{-1} band region are attributed to the Si–O–Si symmetrical stretching and bending motions [51,52]. The band of the sample heat-treated for 8 h shifts to a higher wavenumber (Fig. 4c), likely because the Si-NBO (where NBO is non-bridging oxygen) content in the glass sample after heat-treatment decreases, and the Si–O–Si bond content increases. In turn, this is because the fraction of network modifier Ba^{2+} decreases in the glass matrix after heat treatment and preferentially precipitates in the form of crystal, i.e., the bridging oxygen content increases. The conversion of Si-NBO to Si–O–Si bonds increases the rigidity of the residual glass network. The peaks in the 700-900 cm^{-1} region are assigned to Ti–O* bonds and symmetric stretching between Si and NBO groups, where O* represents the top oxygen of the TiO_5 pyramid [53]. The peak at 860 cm^{-1} is attributed to the short Ti–O bond. As shown in Fig. 4c, the Raman peak in the 8 h heat-treated sample moves to the higher frequency region. Because Ti in the fresnoite crystal is in the five-fold coordinated pyramid structure, the precipitation of the crystal enhances the formation of the TiO_5 pyramid. The peaks in the 900-1200 cm^{-1} band region are assigned to the symmetric Si–O stretching motion [54]. The bands in this region have no obvious shifts. However, we note that two small peaks appear at 561 and 977 cm^{-1}, which may originate from excess SiO_2 in the non-stoichiometric chemical composition of the glass [55].

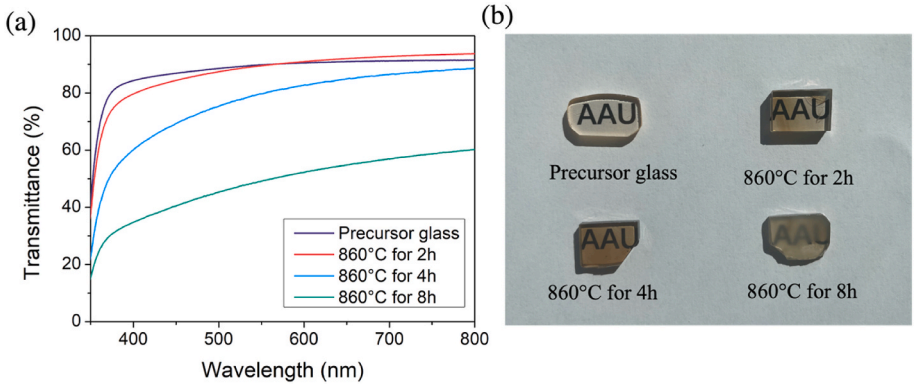

Fig. 5. (a) Transmittance of precursor glass and glass-ceramics samples normalized to a thickness of 1.0 mm and (b) photographs of double polished precursor glass and glass-ceramics samples under visible light.

Table 1
Mechanical properties of BTS glass and glass-ceramics samples. The estimated error for *CR* is 20% of its value.

	Precursor glass	Heat treated 2 h	Heat treated 4 h	Heat treated 8 h
Density (g/cm^3)	3.922 (±0.006)	3.907 (±0.016)	3.938 (±0.011)	3.911 (±0.008)
Hardness (GPa)	5.8 (±0.1)	6.0 (±0.1)	6.4 (±0.4)	6.6 (±0.6)
Young's modulus (GPa)	77.5 (±0.2)	77.6 (±0.7)	78.0 (±1.3)	78.3 (±0.4)
Poisson's ratio	0.269 (±0.01)	0.269 (±0.01)	0.268 (±0.01)	0.268 (±0.01)
Shear modulus (GPa)	30.5 (±0.1)	30.6 (±0.3)	30.8 (±0.7)	30.9 (±0.2)
Bulk modulus (GPa)	55.9 (±0.4)	55.9 (±0.4)	56.1 (±1.2)	56.2 (±0.4)
K_{IFT} (MPa·m$^{1/2}$)	0.77 (±0.03)	0.79 (±0.06)	0.83 (±0.07)	1.00 (±0.06)
K_{Ic_SEPB} (MPa·m$^{1/2}$)	0.73 (±0.11)	0.74 (±0.07)	0.84 (±0.07)	0.91 (±0.08)
CR (N)	0.68	0.54	0.48	0.23

3.2. Transmission properties

The obtained precursor BTS glass was slightly yellowish due to the presence of TiO_2. Studies have shown that the addition of a high fraction of TiO_2 can cause the color of BTS glasses to change from colorless to yellowish to brown [56]. Fig. 5a shows the UV-VIS transmittance spectra of the different samples in the visible range and Fig. 5b shows photographs of the same two-side polished samples. The transmittances of the precursor glass and 2 h heat-treated glass are in the range of 80–91% and 80–93% in the visible range (400-800 nm), respectively. These relatively high values are due to the absence of crystals and the small size of the crystals, respectively. However, when the heat treatment time is prolonged, the transmittance decreases to 60-88% and 34-60% for samples heat-treated for 4 and 8 h, respectively. Combined with the SEM results, the increase of crystal size and content cause increased scattering of light, resulting in a decrease in transmittance due to the refractive index difference between the crystal and glass after heat treatment [57].

3.3. Mechanical properties

Table 1 summarizes the measured mechanical properties of the BTS samples. The density of the four samples does not change and fluctuates around a value of 3.92 g/cm^3. The hardness of glass-ceramics increases with the increase of crystal content (Table 1). Studies have shown that the hardness of non-transparent $40BaO–20TiO_2–40SiO_2$ glass-ceramic with a crystal volume fraction of 54% is nearly 20% higher than that of the precursor glass [31]. Here, the crystal volume fraction of the 8 h heat-treated glass is significantly lower than in this study (as can be seen from the SEM and XRD results), allowing the samples to remain partially transparent, but the increase in hardness is then only about 12%. However, in both cases, the BTS crystals cause an increase in the hardness of the glass-ceramics. This could be due to that both the shear flow [45] and the local densification around the indentation [58] can partially be hindered by the presence of crystals. Nanocrystals drive asymmetric movement of shear flow by confining the expansion of the plastic zone [45], that is, as the residual glass phase content decreases with increasing heat-treatment time, the crystals impede the shear flow and the density around the indent increases [45]. The stresses generated during indenter loading cause the glass structure to reorganize, creating a dense, plastically deformed region. During unloading, in glass-ceramics, the expansion of the elastic region of the indentation is suppressed due to the inhibition of the shear flow by the crystals. This leads to incomplete release of the residual stress generated in the elastic region, and the same phenomenon has also been found to occur in glasses with a higher bulk modulus [59]. The measured hardness value increases due to the reduced amount of elastic recovery in the indented area. The higher hardness of the crystal relative to that of the glass (as expected based on its high modulus, see below) is another reason for the increase in hardness upon crystallization.

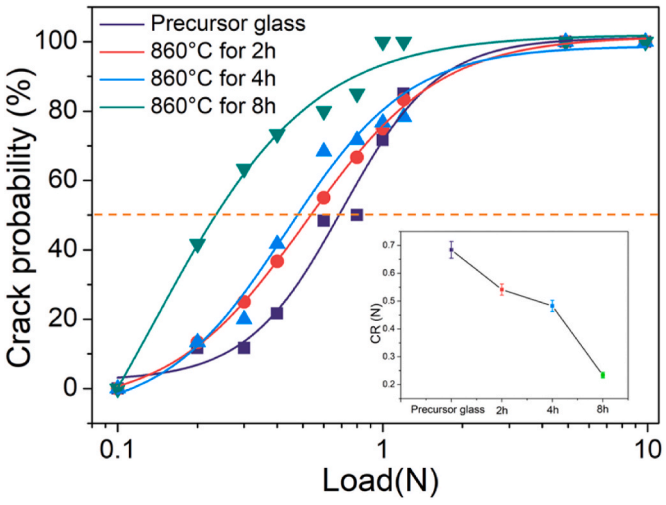

Fig. 6. Crack initiation probability as a function of applied Vickers indentation load for the precursor glass and glass-ceramics. Inset: Crack resistance (*CR*) value.

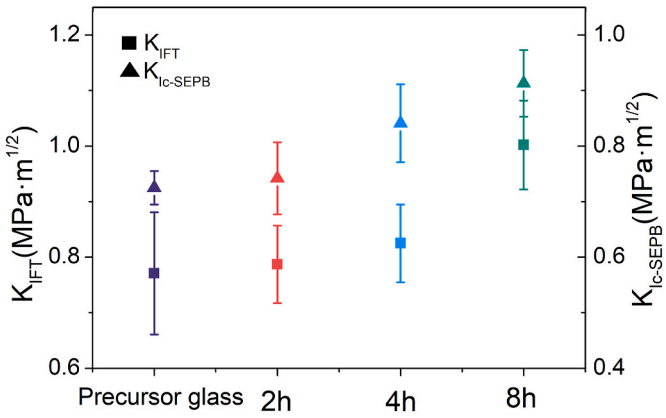

Fig. 7. Fracture toughness of the sample determined using indentation fracture toughness method (K_{IFT}) and single-sided pre-cracked beam method (K_{Ic}).

Regarding the elastic properties, the Young's modulus (*E*), bulk modulus(*K*), and shear modulus (*G*) all increase with the increase of heat-treatment time, whereas Poisson's ratio (ν) decreases (Table 1). The increase in modulus may be due to: (1) the higher modulus of BTS nanocrystals relative to the precursor glass; and (2) the increase in the content of Si–O–Si bonds. Point (1) is supported by the work of Shinozaki et al. [31], who have estimated $E_{nanocrystal} = 125$ GPa, $G_{nanocrystal} = 48$ GPa, and $B_{nanocrystal} = 101$ GPa for $Ba_2TiSi_2O_8$ nanocrystals. In relation to point (2), according to the analysis of the Raman spectroscopy data, the fraction of non-bridging oxygen in the heat-treated samples appears to slightly decrease due to the precipitation of Ba^{2+}. This increases the average bond energy of the residual glass network (Si–O bonds have energy of 443.5 kJ/mol [60]) and the internal network structure of the samples after heat treatment is also more compact, which increases the modulus.

To evaluate the crack initiation resistance, we have determined the *CR* values [61,62]. Fig. 6 shows the crack probability vs. load curves. We find that the crack resistance of the precursor glass is better than that of the glass-ceramics. This decrease in *CR* may be due to the increased packing density of glass-ceramics, considering that the driving force for crack initiation is related to residual stress [63]. Due to the periodic

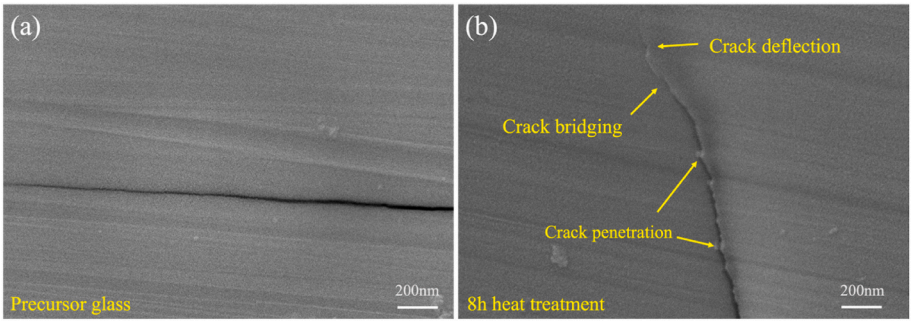

Fig. 8. SEM images of the indentation tip crack path in the (a) precursor glass and (b) the 8 h heat-treated glass-ceramic.

close arrangement of atoms in the crystal, compared with the relatively looser glass structure, the crystal is prone to form more residual stress in the glass-ceramic with the denser atomic packing density under the stress state. In addition, due to the difference in the coefficient of thermal expansion (CTE) between the crystal and the glass, residual stresses will be generated on the surface of the glass upon cooling from the heat-treatment temperature. Such stresses can lead to a greater tendency for crack initiation [64,65]. At the same time, glasses with different crystal contents show different capacities to accommodate strain energy during the indentation process. The softer glass substrate will accommodate more energy, and therefore relatively high crystal content of glasses often tend to be more prone to crack initiation [66].

Fig. 7 shows the fracture toughness values determined using both the indentation and SEPB methods. With the increase in crystal content, the fracture toughness measured by both methods increases. The indentation fracture toughness increases from 0.77 MPa $m^{1/2}$ for the precursor glass to 1.00 MPa $m^{1/2}$ for the 8 h heat-treated sample. In the case of the SEPB method, the corresponding increase is from 0.73 MPa $m^{1/2}$ to 0.91 MPa $m^{1/2}$. It can be seen from the SEM image (Fig. 2) that the crystal orientation on the glass surface varies. Therefore, the crack at the diagonal line of the indentation needs to bypass or pass through the crystal that is inconsistent with the crack propagation direction during the expansion process (see Fig. 8). As such, energy is consumed and the fracture toughness increases [67]. At the same time, the error bars of fracture toughness values obtained by the indentation method are larger for glass-ceramics than precursor glass due to the different number of crystals passing through or bypassing during the crack propagation process, but with the increase of heat treatment time, the increase of fracture toughness is confirmed.

Comparing the fracture toughness values measured by the two methods, it can be found that the fracture toughness values obtained by the SEPB method are lower. Indeed, there is typically a 20%–60% offset between K_{IFT} and K_{Ic}, depending on the chemical composition of the glass [68], as differences in chemical composition lead to differences in atomic packing density and densification deformation [63], and radial cracking is very limited in low Poisson's ratio glasses. Typically, this leads to overestimation of K_{IFT}. The geometry of the indenter also affects the value of K_{IFT}, as a sharper indenter can minimize the effect of indentation-induced densification. In the SEPB method, due to the introduction of pre-cracks, the glass sample breaks along the pre-cracks during the loading process. The tip radius of the propagating crack is made to achieve atomic sharpness, which solves the problem of the roundness of the crack tip or notch width [68]. Therefore, the SEPB method is the preferred method of the two, as it is based on a well-defined crack geometry and benefits from a self-consistent expression of the stress intensity factor [69].

To explore the toughening mechanism, we have obtained SEM images of the indentation tip crack path. Fig. 8 shows the SEM images of the indentation tip crack in the precursor glass and the 8 h heat-treated glass-ceramic. The crack propagation in the precursor glass is not hindered by crystals, resulting in a straight crack propagation path. In the glass-ceramic sample, the formation of crystals leads to deflection and higher tortuosity for crack propagation. Moreover, the driving energy of crack propagation appears to decrease gradually as the crack propagation proceeds, as manifested from the transition from crack penetration to crack bridging to crack deflection, with the fracture mode changing from transgranular to intergranular due to the decrease in fracture energy as the crack propagates [23]. That is, we infer that the crack consumes more energy when passing through the BTS crystal compared to the residual glass phase. As the crack propagates and consumes energy, the crack deflects along the interface between the matrix and the BTS crystal, and the crystal forms a bridge on the main crack, causing crack bridging. The energy is also gradually consumed in the subsequent crack propagation process, causing the deflection of the crack at the front of the crystal until the crack disappears. Overall, compared with the straight cracks in the precursor glass, the crystals in the glass-ceramics effectively inhibit the crack propagation and increase the fracture energy, which increases the fracture toughness.

4. Conclusions

In this paper, we have studied the mechanical and transmission properties of $30BaO–15TiO_2–55SiO_2$ (in mol%) glass-ceramics. With the increase of heat-treatment time, the content and size of crystals in the glass-ceramics increase, and the shape of crystals changes to long strips, which overall reduces the light transmittance. Due to the generation of high modulus fresnoite crystals, the elastic modulus of glass-ceramics increases after heat treatment, whereas the crack initiation resistance decreases because the crystals are harder and more prone to generate residual stress during the indentation process, which leads to a decrease in *CR*. The fracture toughness results show that the indentation fracture toughness is lower than the fracture toughness tested by the SEPB method, but both methods show a pronounced increase upon crystallization. The silicate structure characterized by Raman spectroscopy confirmed the formation of TiO_5 pyramidal crystals and the increase in the fraction of bridging oxygens. The above results confirm that nanocrystals can be used to tune the mechanical properties of glasses, but at the expense of reduced light transmission and crack resistance. This study thus provides guidance for the future preparation of glass-ceramics with large size and content of crystals, highlighting the need to discover crystals with similar refractive index to the residual glass phase to maintain high light transmittance.

Declaration of competing interest

The authors declare that they have no known competing financial interests or personal relationships that could have appeared to influence the work reported in this paper.

Acknowledgement

This work was supported by the China Scholarship Council (CSC No.

202107000016) and the European Union's Horizon 2020 research and innovation programme under the Marie Sklodowska-Curie grant agreement No. 882520.

Appendix A. Supplementary data

Supplementary data to this article can be found online at https://doi.org/10.1016/j.ceramint.2023.02.115.

References

[1] J. Zhong, D. Chen, Y. Peng, Y. Lu, X. Chen, X. Li, Z. Ji, A review on nanostructured glass ceramics for promising application in optical thermometry, J. Alloys Compd. 763 (2018) 34–48, https://doi.org/10.1016/j.jallcom.2018.05.348.

[2] T.K. Pietrzak, M. Wasiucionek, J.E. Garbarczyk, Towards higher electric conductivity and wider phase stability range via nanostructured glass-ceramics processing, Nanomaterials-Basel. 11 (2021) 1321, https://doi.org/10.3390/nano11051321.

[3] M. Montazerian, M. Mancini, J.C. Mauro, Advanced tools for unveiling nucleation in nanostructured glass-ceramics, Crit. Rev. Solid. State. (2022) 1–29, https://doi.org/10.1080/10408436.2022.2066624.

[4] X. Lin, H. Liang, T. Liu, P. Zhang, X. Jiang, Y. Yu, T. Ning, A. Lu, Preparation, structure and optical properties of Nd_2O_3 doped Gd_2O_3-Ga_2O_3-GeO_2 transparent glass-ceramics containing novel $GdGaGe_2O_7$ nanocrystal, J. Eur. Ceram. Soc. 42 (2022) 6135–6145, https://doi.org/10.1016/j.jeurceramsoc.2022.05.071.

[5] F. Hu, H. Gong, R. Wei, H. Guo, Reproducible X-ray excited luminescence performance with transparent Tb^{3+}-doped $NaGd_2F_7$ scintillating glass ceramics, J. Eur. Ceram. Soc. 42 (2022) 6654–6662, https://doi.org/10.1016/j.jeurceramsoc.2022.07.018.

[6] P.S. Bechthold, S. Haussühl, E. ' Michael, J. Eckstein, K. Recker, F. Wallrafen, Second harmonic generation in fresnoite, $Ba_2TiSi_2O_8$, Phys. Lett. 65 (1978) 453–454, https://doi.org/10.1016/0375-9601(78)90469-3.

[7] Y. Takahashi, K. Kitamura, Y. Benino, T. Fujiwara, T. Komatsu, Second-order optical nonlinear and luminescent properties of $Ba_2TiSi_2O_8$ nanocrystallized glass, Appl. Phys. Lett. 86 (2005), 091110, https://doi.org/10.1063/1.1879114.

[8] M.C. Foster, D.J. Arbogast, R.M. Nielson, P. Photinos, S.C. Abrahams, Fresnoite: a new ferroelectric mineral, J. Appl. Phys. 85 (1999) 2299–2303, https://doi.org/10.1063/1.369541.

[9] Glass-ceramics, A class of nanostructured materials for photonics, La Rivista Del Nuovo Cimento 38 (2015) 311–369, https://doi.org/10.1393/ncr/i2015-10114-0.

[10] T. Komatsu, T. Honma, Optical active nano-glass-ceramics, Int. J. Appl. Glass Sci. 4 (2013) 125–135, https://doi.org/10.1111/ijag.12023.

[11] M. Clara Gonçalves, L.F. Santos, R.M. Almeida, Rare-earth-doped transparent glass ceramics, Compt. Rendus Chem. 5 (2002) 845–854, https://doi.org/10.1016/S1631-0748(02)01457-1.

[12] T. Yamazawa, T. Honma, H. Suematsu, T. Komatsu, Synthesis, ferroelectric and electrooptic properties of transparent crystallized glasses with $Sr_xBa_{1-x}Nb_2O_6$ nanocrystals, J. Am. Ceram. Soc. 92 (2009) 2924–2930, https://doi.org/10.1111/j.1551-2916.2009.03348.x.

[13] X. Liu, J. Zhou, S. Zhou, Y. Yue, J. Qiu, Transparent glass-ceramics functionalized by dispersed crystals, Prog. Mater. Sci. 97 (2018) 38–96, https://doi.org/10.1016/j.pmatsci.2018.02.006.

[14] T. Berthier, V.M. Fokin, E.D. Zanotto, New large grain, highly crystalline, transparent glass–ceramics, J. Non-Cryst. Solids 354 (2008) 1721–1730, https://doi.org/10.1016/j.jnoncrysol.2007.08.052.

[15] M. Ghasemzadeh, A. Nemati, S. Baghshahi, Effects of nucleation agents on the preparation of transparent glass–ceramics, J. Eur. Ceram. Soc. 32 (2012) 2989–2994, https://doi.org/10.1016/j.jeurceramsoc.2012.02.055.

[16] T. Berthier, V.M. Fokin, E.D. Zanotto, New large grain, highly crystalline, transparent glass–ceramics, J. Non-Cryst. Solids 354 (2008) 1721–1730, https://doi.org/10.1016/j.jnoncrysol.2007.08.052.

[17] M.A.P. Silva, Y. Messaddeq, V. Briois, M. Poulain, F. Villain, S.J.L. Ribeiro, Synthesis and structural investigations on TeO_2-PbF_2-CdF_2 glasses and transparent glass-ceramics, J. Phys. Chem. Solid. 63 (2002) 605–612, https://doi.org/10.1016/S0022-3697(01)00200-1.

[18] L. Han, J. Song, C. Lin, J. Liu, T. Liu, Q. Zhang, Z. Luo, A. Lu, Crystallization, structure and properties of MgO-Al_2O_3-SiO_2 highly crystalline transparent glass-ceramics nucleated by multiple nucleating agents, J. Eur. Ceram. Soc. 38 (2018) 4533–4542, https://doi.org/10.1016/j.jeurceramsoc.2018.05.025.

[19] B. Rangarajan, S.S.N. Bharadwaja, E. Furman, T. Shrout, M. Lanagan, Impedance spectroscopy studies of fresnoites in BaO-TiO_2-SiO_2 system, J. Am. Ceram. Soc. 93 (2010) 522–530, https://doi.org/10.1111/j.1551-2916.2009.03423.x.

[20] T. Honma, T. Komatsu, Y. Benino, Patterning of *c*- axis-oriented $Ba_2TiX_2O_8$ (X = Si, Ge) crystal lines in glass by laser irradiation and their second-order optical nonlinearities, J. Mater. Res. 23 (2008) 885–888, https://doi.org/10.1557/jmr.2008.0135.

[21] Y. Luo, C. Qu, J.C. Mauro, High toughness transparent glass-ceramics with petalite and β-spodumene solid solution as two major crystal phases, J. Am. Ceram. Soc. 105 (2022) 6116–6127, https://doi.org/10.1111/jace.18590.

[22] L. Sant'Ana Gallo, F. Célarié, J. Bettini, A.C.M. Rodrigues, T. Rouxel, E.D. Zanotto, Fracture toughness and hardness of transparent MgO–Al_2O_3–SiO_2 glass-ceramics, Ceram. Int. 48 (2022) 9906–9917, https://doi.org/10.1016/j.ceramint.2021.12.195.

[23] Q. Fu, E.M. Aaldenberg, E.N. Coon, T.M. Gross, A.M. Whittier, B.M. Abel, D. E. Baker, Tough, bioinspired transparent glass-ceramics, Adv. Eng. Mater. (2022), 2200350, https://doi.org/10.1002/adem.202200350.

[24] W. Wisniewski, F. Döhler, C. Rüssel, Oriented nucleation and crystal growth of Ba-Fresnoite ($Ba_2TiSi_2O_8$) in 2BaO·TiO_2 ·2 SiO_2 glasses with additional SiO_2, Cryst. Growth Des. 18 (2018) 3202–3208, https://doi.org/10.1021/acs.cgd.8b00312.

[25] N. Maruyama, T. Honma, T. Komatsu, Electronic polarizability and Judd–Ofelt parameters of Nd^{3+} and Er^{3+} ions in transparent crystallized glasses with nonlinear optical $Ba_2TiSi_2O_8$ nanocrystals, J. Chem. Phys. 128 (2008), 184706, https://doi.org/10.1063/1.2908231.

[26] H. Masai, G. Okada, N. Kawaguchi, T. Yanagida, Photoluminescence and X-ray-induced scintillation of BaO-TiO_2-SiO_2 glasses and the glass-ceramics, J. Non-Cryst. Solids 501 (2018) 131–135, https://doi.org/10.1016/j.jnoncrysol.2017.11.026.

[27] H.K. Lee, Y. Su Lee, A.S. Bhalla, W.H. Kang, Preparation and properties of transparent glass-ceramics in *x*K_2O-(33.3- *x*)BaO-16.7TiO_2 -50SiO_2 Glasses, Ferroelectrics 330 (2006) 9–18, https://doi.org/10.1080/00150190600605361.

[28] B. Zhu, B. Qian, Y. Liu, C. Xu, C. Liu, Q. Chen, J. Zhou, X. Liu, J. Qiu, A volumetric full-color display realized by frequency upconversion of a transparent composite incorporating dispersed nonlinear optical crystals, NPG Asia Mater. 9 (2017), https://doi.org/10.1038/am.2017.89 e394–e394.

[29] N. Toyohara, Y. Benino, T. Fujiwara, T. Komatsu, Enhancement of second harmonic intensity in thermally poled ferroelectric nanocrystallized glasses in the BaO–TiO_2–SiO_2 system, Solid State Commun. 140 (2006) 299–303, https://doi.org/10.1016/j.ssc.2006.08.030.

[30] H. Masai, N. Iwafuchi, Y. Takahashi, T. Fujiwara, S. Ohara, Y. Kondo, N. Sugimoto, Preparation of crystallized glass for application in fiber-type devices, J. Mater. Res. 24 (2009) 288–294, https://doi.org/10.1557/JMR.2009.0021.

[31] K. Shinozaki, T. Honma, T. Komatsu, Elastic properties and Vickers hardness of optically transparent glass–ceramics with fresnoite $Ba_2TiSi_2O_8$ nanocrystals, Mater. Res. Bull. 46 (2011) 922–928, https://doi.org/10.1016/j.materresbull.2011.02.031.

[32] E.M. Ghardi, A. Atila, M. Badawi, A. Hasnaoui, S. Ouaskit, Computational insights into the structure of barium titanosilicate glasses, J. Am. Ceram. Soc. 102 (2019) 6626–6639, https://doi.org/10.1111/jace.16536.

[33] Y. Rho, S. Kang, Nanometer scale microstructure and optical properties of BaO–TiO_2 –SiO_2 system-based glass-ceramics, J. Nanosci. Nanotechnol. 20 (2020) 324–330, https://doi.org/10.1166/jnn.2020.17289.

[34] R. Keding, C. Rüssel, Oriented glass-ceramics containing fresnoite prepared by electrochemical nucleation of a BaO–TiO_2–SiO_2–B_2O_3 melt, J. Non-Cryst. Solids 278 (2000) 7–12, https://doi.org/10.1016/S0022-3093(00)00338-0.

[35] H.K. Lee, Y.S. Lee, A.S. Bhalla, W.H. Kang, The effect of K_2O in the glass–ceramics based on the BaO–TiO_2–SiO_2 glasses, Mater. Lett. 60 (2006) 2457–2460, https://doi.org/10.1016/j.matlet.2006.01.018.

[36] P. Liu, K. Januchta, L.R. Jensen, M. Bauchy, M.M. Smedskjaer, Competitive effects of free volume, rigidity, and self-adaptivity on indentation response of silicoaluminoborate glasses, J. Am. Ceram. Soc. 103 (2020) 944–954, https://doi.org/10.1111/jace.16790.

[37] K.F. Frederiksen, K. Januchta, N. Mascaraque, R.E. Youngman, M. Bauchy, S. J. Rzoska, M. Bockowski, M.M. Smedskjaer, Structural compromise between high hardness and crack resistance in aluminoborate glasses, J. Phys. Chem. B 122 (2018) 6287–6295, https://doi.org/10.1021/acs.jpcb.8b02905.

[38] P. Liu, R.E. Youngman, L.R. Jensen, M. Bockowski, M.M. Smedskjaer, Achieving ultrahigh crack resistance in glass through humid aging, Phys. Rev. Materials. 4 (2020), 063606, https://doi.org/10.1103/PhysRevMaterials.4.063606.

[39] T.M. Gross, H. Liu, Y. Zhai, L. Huang, J. Wu, The impact of densification on indentation fracture toughness measurements, J. Am. Ceram. Soc. 103 (2020) 3920–3929, https://doi.org/10.1111/jace.16793.

[40] S. Yoshida, J.-C. Sanglebœuf, T. Rouxel, Quantitative evaluation of indentation-induced densification in glass, J. Mater. Res. 20 (2005) 3404–3412, https://doi.org/10.1557/jmr.2005.0418.

[41] X. Ren, T. Du, H. Peng, L.R. Jensen, C.A.N. Biscio, L. Fajstrup, M. Bauchy, M. M. Smedskjaer, Irradiation-induced toughening of calcium aluminoborosilicate glasses, Mater. Today Commun. 31 (2022), 103649, https://doi.org/10.1016/j.mtcomm.2022.103649.

[42] T. To, S.S. Sørensen, M. Stepniewska, A. Qiao, L.R. Jensen, M. Bauchy, Y. Yue, M. M. Smedskjaer, Fracture toughness of a metal–organic framework glass, Nat. Commun. 11 (2020) 2593, https://doi.org/10.1038/s41467-020-16382-7.

[43] T. To, F. Célarié, C. Roux-Langlois, A. Bazin, Y. Gueguen, H. Orain, M. Le Fur, V. Burgaud, T. Rouxel, Fracture toughness, fracture energy and slow crack growth of glass as investigated by the Single-Edge Precracked Beam (SEPB) and Chevron-Notched Beam (CNB) methods, Acta Mater. 146 (2018) 1–11, https://doi.org/10.1016/j.actamat.2017.11.056.

[44] T. To, S.S. Sørensen, J.F.S. Christensen, R. Christensen, L.R. Jensen, M. Bockowski, M. Bauchy, M.M. Smedskjaer, Bond switching in densified oxide glass enables record-high fracture toughness, ACS Appl. Mater. Interfaces 13 (2021) 17753–17765, https://doi.org/10.1021/acsami.1c00435.

[45] B. Deng, J. Luo, J.T. Harris, C.M. Smith, T.M. Wilkinson, Toward revealing full atomic picture of nanoindentation deformation mechanisms in Li_2O-2SiO_2 glass-ceramics, Acta Mater. 208 (2021), 116715, https://doi.org/10.1016/j.actamat.2021.116715.

[46] P. Patra, K. Annapurna, Transparent tellurite glass-ceramics for photonics applications: a comprehensive review on crystalline phases and crystallization mechanisms, Prog. Mater. Sci. 125 (2022), 100890, https://doi.org/10.1016/j.pmatsci.2021.100890.

[47] D.S. Patil, M. Konale, M. Gabel, O.K. Neill, J.V. Crum, A. Goel, M.C. Stennett, N. C. Hyatt, J.S. McCloy, Impact of rare earth ion size on the phase evolution of MoO_3-

containing aluminoborosilicate glass-ceramics, J. Nucl. Mater. 510 (2018) 539–550, https://doi.org/10.1016/j.jnucmat.2018.08.004.
[48] W. Wisniewski, M. Patschger, C. Rüssel, Sr-fresnoite surface crystallisation in a 2SrO·TiO_2·2.75 SiO_2 glass studied by EBSD, CrystEngComm 14 (2012) 5425, https://doi.org/10.1039/c2ce25117e.
[49] H. Masai, Structure studies of BaO-TiO_2-SiO_2 glass-ceramics using ^{29} Si MAS NMR and Raman spectroscopy, BCSJ 91 (2018) 950–956, https://doi.org/10.1246/bcsj.20180011.
[50] H. Masai, S. Tsuji, T. Fujiwara, Y. Benino, T. Komatsu, Structure and non-linear optical properties of BaO–TiO_2–SiO_2 glass containing $Ba_2TiSi_2O_8$ crystal, J. Non-Cryst. Solids 353 (2007) 2258–2262, https://doi.org/10.1016/j.jnoncrysol.2007.03.005.
[51] S.A. Markgraf, S.K. Sharma, A.S. Bhalla, Raman study of glasses of $Ba_2TiSi_2O_8$ and $Ba_2TiGe_2O_8$, J. Am. Ceram. Soc. 75 (1992) 2630–2632, https://doi.org/10.1111/j.1151-2916.1992.tb05629.x.
[52] S.A. Markgraf, S.K. Sharma, A.S. Bhalla, Raman study of fresnoite-type materials: polarized single crystal, crystalline powders, and glasses, J. Mater. Res. 8 (1993) 635–648, https://doi.org/10.1557/JMR.1993.0635.
[53] T.H. Kim, Y.S. Kim, Y.J. Jeong, Y.H. Na, H.H. Lim, M.S. Cha, B.K. Ryu, Optical properties and structure of BaO-TiO2-SiO2 glass ceramics, J. Korean Ceram. Soc. 45 (2008) 821–826, https://doi.org/10.4191/KCERS.2008.45.1.821.
[54] V. McMillan, D.E. Galvez-Aranda, J.M. Seminario, Structural studies of silicate glasses and melts—applications and limitations of Raman spectroscopy, Am. Mineral 69 (1984) 622–644.
[55] Y. Takahashi, Y. Benino, T. Fujiwara, T. Komatsu, Large second-order optical nonlinearities of fresnoite-type crystals in transparent surface-crystallized glasses, J. Appl. Phys. 95 (2004) 3503–3508, https://doi.org/10.1063/1.1664022.
[56] P. Mezeix, F. Célarié, P. Houizot, Y. Gueguen, F. Muñoz, T. Rouxel, Elasticity and viscosity of BaO TiO2SiO2 glasses in the 0.9 to 1.2Tg temperature interval, J. Non-Cryst. Solids 445–446 (2016) 45–52, https://doi.org/10.1016/j.jnoncrysol.2016.05.006.
[57] Z. Li, C. Chen, W. Shen, D. Zhou, L.R. Jensen, X. Qiao, J. Ren, J. Du, Y. Zhang, J. Qiu, Y. Yue, The transformation from translucent into transparent rare earth ions doped oxyfluoride glass-ceramics with enhanced luminescence, Adv. Opt. Mater. 10 (2022), 2102713, https://doi.org/10.1002/adom.202102713.
[58] F.M. Ernsberger, Role of densification in deformation of glasses under point loading, J. Am. Ceram. Soc. 51 (1968) 545–547, https://doi.org/10.1111/j.1151-2916.1968.tb13318.x.
[59] K. Januchta, P. Liu, S.R. Hansen, T. To, M.M. Smedskjaer, Indentation cracking and deformation mechanism of sodium aluminoborosilicate glasses, J. Am. Ceram. Soc. 103 (2020) 1656–1665, https://doi.org/10.1111/jace.16894.
[60] V. Dimitrov, T. Komatsu, Average single bond strength and optical basicity of Na_2O-GeO_2 glasses, J. Ceram. Soc. Japan. 117 (2009) 1105–1111, https://doi.org/10.2109/jcersj2.117.1105.
[61] G.A. Rosales-Sosa, A. Masuno, Y. Higo, H. Inoue, Crack-resistant Al_2O_3–SiO_2 glasses, Sci. Rep. 6 (2016), 23620, https://doi.org/10.1038/srep23620.
[62] M. Wada, H. Furukawa, K. Fujita, Crack resistance of glass on Vickers indentation, Proc. Int. Congr. Glass. 11 (1974) 39–46.
[63] K. Januchta, R.E. Youngman, L.R. Jensen, M.M. Smedskjaer, Mechanical property optimization of a zinc borate glass by lanthanum doping, J. Non-Cryst. Solids 520 (2019), 119461, https://doi.org/10.1016/j.jnoncrysol.2019.119461.
[64] D. Li, J.W. Guo, X.S. Wang, S.F. Zhang, L. He, Effects of crystal size on the mechanical properties of a lithium disilicate glass-ceramic, Mater. Sci. Eng. 669 (2016) 332–339, https://doi.org/10.1016/j.msea.2016.05.068.
[65] D.C.N. Fabris, E.H. Miguel, R. Vargas, R.B. Canto, M. de O.C. Villas-Boas, O. Peitl, V.M. Sglavo, E.D. Zanotto, Microstructure, residual stresses, and mechanical performance of surface crystallized translucent glass-ceramics, J. Eur. Ceram. Soc. 42 (2022) 4631–4642, https://doi.org/10.1016/j.jeurceramsoc.2022.04.024.
[66] X. Hao, X. Hu, Z. Luo, T. Liu, Z. Li, T. Wu, A. Lu, Y. Tang, Preparation and properties of transparent cordierite-based glass-ceramics with high crystallinity, Ceram. Int. 41 (2015) 14130–14136, https://doi.org/10.1016/j.ceramint.2015.07.034.
[67] K.G. Aakermann, K. Januchta, J.A.L. Pedersen, M.N. Svenson, S.J. Rzoska, M. Bockowski, J.C. Mauro, M. Guerette, L. Huang, M.M. Smedskjaer, Indentation deformation mechanism of isostatically compressed mixed alkali aluminosilicate glasses, J. Non-Cryst. Solids 426 (2015) 175–183, https://doi.org/10.1016/j.jnoncrysol.2015.06.028.
[68] T. Rouxel, S. Yoshida, The fracture toughness of inorganic glasses, J. Am. Ceram. Soc. 100 (2017) 4374–4396, https://doi.org/10.1111/jace.15108.
[69] T. Nose, T. Fujii, Evaluation of fracture toughness for ceramic materials by a Single-Edge-Precracked-Beam method, J. Am. Ceram. Soc. 71 (1988) 328–333, https://doi.org/10.1111/j.1151-2916.1988.tb05049.x.